



Instrument Science Report WFC3 2015-18

Spatial Accuracy of the UVIS Flat Fields

J. Mack, A. Rajan, & A. S. Bowers

December 30, 2015

ABSTRACT

To quantify the accuracy of the UVIS flat fields, subarray observations in eight filters of bright HST standard stars were stepped across the detector field of view. For filters with pivot wavelength greater than 300nm, photometry in a 10-pixel aperture is repeatable to better than 0.7% rms and 2.7% peak-to-peak. The flux residual shows a weak correlation with the number of y-transfers, indicating that some of the spatial variation is due to CTE losses during readout. For UV filters (pivot wavelength less than 300nm), the photometric residuals are 1.8% rms and 6.7% peak-to-peak. Flats for these four filters were acquired in ambient conditions during ground testing, so these large residuals, which correspond to a crosshatch pattern in the flats, were expected. The UV photometry also shows offsets between the two UVIS chips of up to 5% for the bluest filters. These offsets are attributed to color differences between the blue HST standards and the average color of Omega Cen, which was used to compute inflight corrections to the ground flats. Using cluster observations with an orientation difference of 95 degrees, photometric offsets between chips are quantified for different stellar populations selected by color from the UV color magnitude diagram of Omega Cen. The measured offset between chips for 'blue' versus 'yellow' is consistent with the offset in the stepped data. A model correcting the UV flats using the stepped photometry will be described in a forthcoming ISR.

I. Introduction

A revised set of UVIS flat fields was delivered to the HST archive on December 14, 2011. These improved reference files include two major corrections to the ground test flats, including the removal of a large-scale internal reflection (or 'flare') and a residual correction for low-frequency (L-flat) sensitivity differences computed from inflight star cluster observations (Mack et al. 2013). The flare correction was based on a geometric model of the light path tracing the four internal reflections (McCullough 2011), and the

remaining low-frequency sensitivity residuals were derived from high signal-to-noise observations of stars in Omega Cen dithered across the detector in 10 broadband filters obtained over ~ 2 years at a range of orientations. Noting the general wavelength-dependence of both the flare and the L-flat, the combined correction for the remaining 32 full-frame UVIS filters was interpolated from the 10 broadband filters using the filter pivot wavelength. Each flat field was then normalized to a small region on UVIS1, preserving any sensitivity offsets between chips derived from the dithered star cluster observations.

To verify the accuracy of the 2011 flat fields, a new calibration program observed bright HST standards on different portions of the detector to quantify any spatial variability in the photometry. High signal-to-noise observations of a single source stepped over many positions provides a complementary strategy to the dithered star cluster observations. Making use of small subarrays, it is possible to fit as many as 20 separate exposures into a single orbit, making this an efficient approach. While the cluster allows thousands of independent measurements per frame, the stars are much fainter and are therefore more susceptible to CTE losses than the much brighter HST standards. Additionally, the dense cluster environment may introduce unknown systematics in the photometry due to crowding, so the bright standards provide an excellent cross-check of the L-flat solutions.

This report highlights the results of stepped photometry obtained over four cycles of WFC3 calibration. Observations were obtained in eight UVIS filters covering the full wavelength range of the detector. Section 2 describes the observing strategy for each program, including the choice of HST standards and portions of the detector sampled for each filter. Sections 3 and 4 describe the aperture photometry and spatial repeatability measured in both calibrated and drizzled frames. Section 5 quantifies the impact of CTE losses on the spatial residuals, and Section 6 considers the effect of spectral type on the flux offset measured between the two UVIS chips in the UV filters.

II. Observations

The four photometric stepping programs are summarized in Table 1. The first program (12090) was designed to better understand the observed throughput in the F336W filter. Kalirai *et al.* (2009) noted that counts measured in this filter were systematically $\sim 5\%$ higher than expected based on a smooth fit to the on-orbit correction with wavelength. The photometric monitoring programs used small 512x512 subarrays in the corners of UVIS1 and UVIS2, and the WFC3 team proposed stepping those same subarrays across the detector to understand whether this filter was simply more efficient than expected or if the flat field was somehow less accurate in the corner of the detector. Stepping was performed in a regular grid pattern shown in Figure 1 using the same white dwarf standard GD153 ($V=13.35$) as used in photometric calibration program 11450.

The stepped data from program 12090 were important in validating the accuracy of the 2011 flats fields prior to delivery. Using a preliminary version of the inflight flat correction, aperture photometry of GD153 in a 10-pixel radius showed spatial residuals of $\pm 1\%$ in a systematic pattern across the detector. The L-flats, on the other hand, were derived from cluster photometry in a 5-pixel aperture to minimize the effects of crowding. Sabbi & Bellini (2013) used the same Omega Cen data to demonstrate the need to correct sources

for both spatial and temporal variations of the PSF inside 10 pixels ($\sim 0.4''$). Once the required aperture corrections were applied and the L-flats recomputed, the spatial pattern in the stepped white dwarf photometry disappeared (Mack et al. 2013, Figure 10), validating the improved F336W flats to $\pm 0.8\%$ accuracy for any region on the detector.

Building on the success of this initial program, additional stepped observations were obtained in program 12707 over the full wavelength range of the detector in four popular broadband filters: F275W, F438W, F606W, and F814W. A brighter white dwarf standard, G191B2B ($V=11.78$) was selected to make the observing program more efficient by reducing the required exposure time for the F225W and F438W filters. Unfortunately, this required the F606W filter to have short 0.7 second exposures for which shutter repeatability tests have shown variations of $\sim 2\%$ in the actual exposure duration (Hilbert 2010).

Detector positions for this new program were selected to step across known ‘features’ in the flats. For example, to verify that the UVIS flare was adequately removed in the 2011 flats, the white dwarf was placed on regions containing the superposition of 1 to 4 of the wedge-shaped reflections (Figure 2). This would provide some check on the shape of the flare model (for example the opening angle) used to correct the ground flats and also the strength of the flare with wavelength as determined from cluster photometry. The white dwarf was also stepped across a low sensitivity region in quadrant D at the bottom of UVIS2. This large, diffuse spot is seen in the flats at wavelengths greater than $\sim 600\text{nm}$ and where the silicon detector layer is up to 2 microns thinner than the surrounding region (Wong 2010).

Early results from the F606W filter showed variations in photometry of $\pm 2\%$, much higher than for the other broad filters. To test whether this was due to limitations in shutter repeatability, a repeat of one orbit was requested in program 13096 using the fainter white dwarf standard GD71 ($V=13.03$) and longer 2.0 second exposures sampling a subset of the original detector positions.

The F275W filter also showed large photometric residuals correlated with mid-frequency structure in the flats for blue filters, originally referred to as a ‘crosshatch’ pattern by Baggett (2007) and as a ‘quilt’ pattern by Sabbi (2008). Flats for the UV filters (F218W, F225W, F275W, and F280N) had been obtained in ambient conditions during ground testing (Sabbi et al. 2009), so large residuals in were expected and were presumed to exist at similar levels for the other three UV filters. For this reason, additional stepped observations in the popular F225W filter were obtained in program 13096. This time, detector positions were carefully selected to place the white dwarf on pixels with reduced sensitivity in the flat (dark regions in Figure 3). A similar number of both low and high sensitivity regions were sampled to determine if a simple model could be computed to correct the UV flats for the observed crosshatch residuals.

Stepped observations in the two remaining UV filters, F218W and F280N, were obtained in calibration program 13584, sampling the same detector positions as for the F225W filter. Since the UVIS1 chip is $\sim 30\%$ less sensitive in F218W than UVIS2, the exposure time was increased for this chip (see Table 1) in order to achieve a similar signal-to-noise of ~ 500 on both chips. For F280N, the UVIS2 chip is only 2% less sensitive, so the exposure time was kept fixed for the two chips. We returned to the white dwarf standard G191B2B for F218W but used the brighter HST standard BD+75D325 ($V=9.55$, spectral type O5p) for the narrow F280N filter to reduce the exposure time required to achieve $S/N \sim 500$. Noting CTE

tails in subarray observations taken far from the amplifiers, the latter two calibration programs (13096 and 13584) added post-flash to the observations at a level of 12 electrons. Anderson et al. (2012) recommend this as an optimal background level for mitigating losses due to CTE.

Using optional APT parameters available only in special ‘Engineering Mode’**, custom subarrays were defined to position the target on a specific set of detector pixels for each program. To achieve this, the star position was offset from the geometric center of each chip (aperture=UVIS1-FIX, UVIS2-FIX) by some computed set of x/y shifts in detector space, converted to offsets on the sky (POSTARG1, POSTARG2) in arcseconds using a model of the geometric distortion.

For each stepping program, two observations were obtained at each detector position using the WFC3-UVIS-DITHER-LINE pattern. The ‘two-point line’ is preferred to a standard ‘cosmic-ray split’ pair because it also allows for rejection of detector artifacts such as bad columns and hot pixels when the pairs are combined with AstroDrizzle. For the first two programs (12090 and 12707), the point spacing was set to 0.290” (7.3 pixels) along a 46.8 degree diagonal. For the later two programs (13096 and 13584) which were intended to sample the UV crosshatch pattern, the point spacing was reduced to 0.145” (3.7 pixels) to make it less likely for the star to move between regions of low and high sensitivity due to the line dither.

Table 1. WFC3/UVIS stepping programs.

Prop	PI	Date	Filters	Target	Spec Type	Vmag	Exptime (sec)	Total Steps	Post-Flash
12090	Kalirai	July 2010	F336W	GD153	WD	13.35	5.4	46	--
12707	Rajan	Dec 2011 Feb 2012	F275W F438W F606W F814W	G191B2B	WD	11.78	1.5 1.3 0.7 3.0	50	--
13096	Mack	Jan 2013	F225W F606W	GD71	WD	13.03	3.3 2.0	44 20	12e-
13584	Mack	Jan 2014 Mar 2014	F218W F280N	G191B2B BD+75D325	WD O5p	11.78 9.55	2.5, 1.9* 2.6	44	12e-

*UVIS1 (2.5s), UVIS2 (1.9s).

**CENTERAXIS1=TARGET, CENTERAXIS2=TARGET, SIZEAXIS1=512, SIZEAXIS2=512

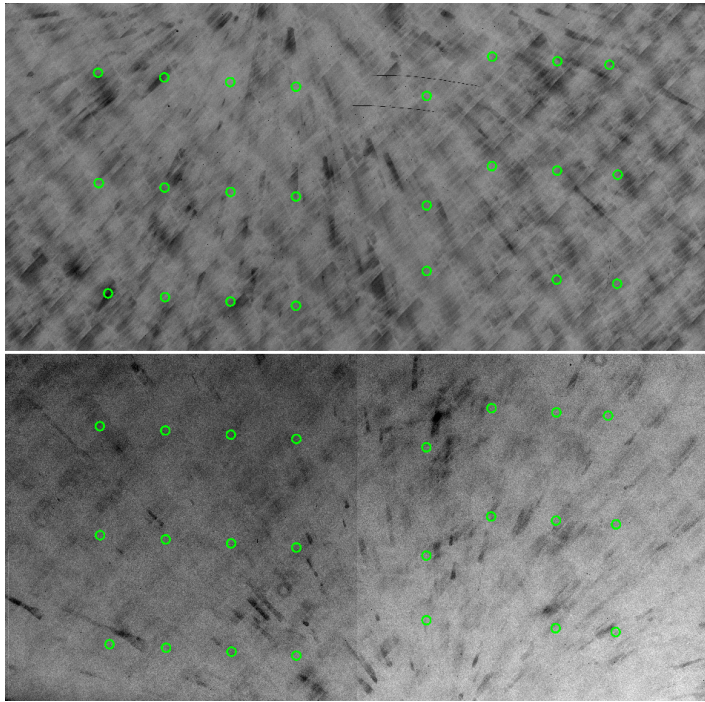


Figure 1: Stepped positions for program 12090 superposed onto an image of the F336W flat field, with UVIS1 at the top and UVIS2 at the bottom. Black indicates regions of the detectors with lower sensitivity. The observations sampled a regular grid across the detector to test for spatial variability in the flat field.

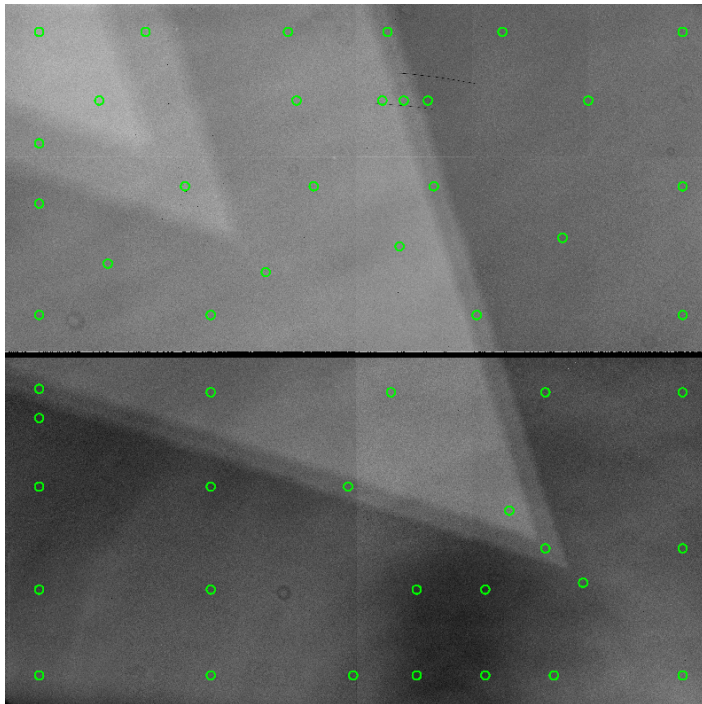


Figure 2: Stepped positions for program 12707 (F275W, F438W, F606W, F814W) superposed onto a co-added image of the F814W flat field plus a scaled geometric model of the UVIS flare. Detector positions were selected to sample various regions of the flare as well as the dark, low sensitivity region in UVIS2 where the chip is thinner than the surrounding region.

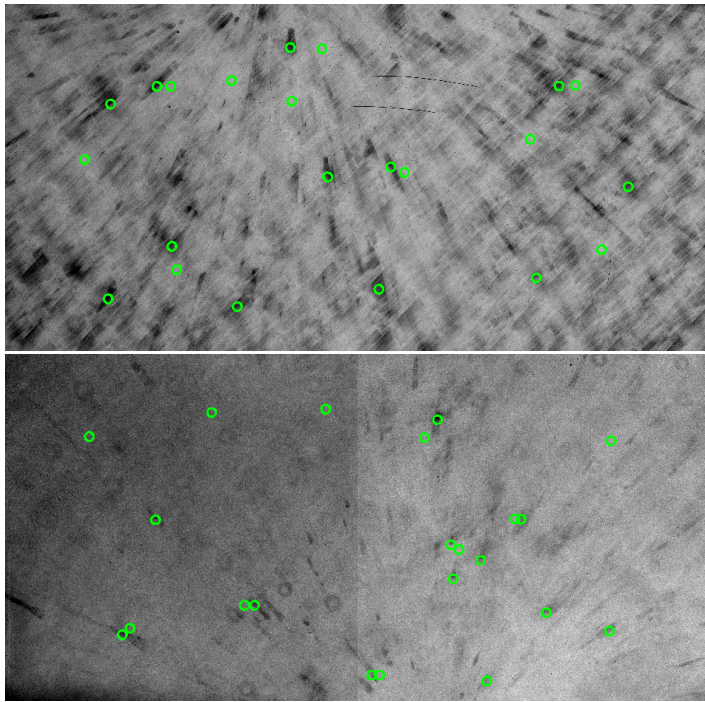


Figure 3: Stepped positions for programs 13096 and 13584 (F218W, F225W, & F280N) superposed onto an image of the F225W flat field. Care was taken to precisely place the star on low (dark) and high (light) sensitivity regions of the UV crosshatch pattern.

III. Aperture Photometry

Raw subarray frames were calibrated with CALWF3 which subtracts the bias, dark, and post-flash, divides by the flat field, and multiplies by the gain to produce calibrated data products in units of electrons. Aperture photometry was performed on both the individual ‘*flt.fits’ (FLT) exposures, multiplied by the appropriate region of the UVIS pixel area map (PAM) to correct for varying pixel area (Kalirai et al. 2010), as well as on the drizzle-combined pairs.

To convert subarray positions to full-frame coordinates, the python code ‘subarray_regions.py’, written by team member H. Bushouse, was used to determine the corresponding region of the pixel area map required to correct each custom subarray. The code has been adapted to print the PyRAF syntax for calling ‘imcalc’ to correct each image and has been included in Appendix B. This software is also useful for mapping subarray coordinates to full frame coordinates by returning the (x,y) value of the lower-left corner of the subarray. The position of the star in the full-frame image may then be computed by adding the position of the subarray corner to the star’s observed position in the subarray.

Next, the IRAF/DAOPHOT task ‘phot’ was used to compute aperture photometry. Because the selected HST standards have no close neighbors, photometry was performed in a range of apertures ranging from 5 to 20 pixels, using the mode of the sky background in an annulus from 75-125 pixels. The star was measured twice at each detector position, offset by only a few pixels, so for FLT products, the average of the two flux measurements was then computed.

For comparison, aperture photometry was also performed on drizzled data products, where AstroDrizzle was used to correct the observations for geometric distortion, flag cosmic-rays and combine pairs of exposures. Our initial results showed that some pairs drizzled of images produced higher photometric residuals than the average of the two FLT*PAM measurements. A careful examination of those drizzled products showed that the default AstroDrizzle parameters for WFC3/UVIS can occasionally produce highly skewed results when combining pairs of images. Specifically, when the star falls on the corner of a pixel in one image and on the center of a pixel in the second image, the latter will have a significantly sharper PSF and may be misidentified as a cosmic-ray. The flagged pixel will be replaced with the lower peak from the second image, resulting in photometry that is too faint in the combined image. Additionally, when a flagged hot pixel is adjacent to the PSF core, where the slope of the radial profile is changing rapidly, rejecting that pixel can do more harm than good by filling in that pixel with portions of overlapping, neighboring pixels. Both effects are described in detail by Mack (2016a, in prep).

IV. Results

When a source is observed at various locations on the detector, its photometric repeatability is an indicator of the flat field accuracy. The figures in Appendix A map the percent variation at each stepped position relative to the mean flux across the detector for each filter. For the flats obtained under vacuum conditions at the inflight temperature (F336W, F438W, F606W, F814W), the color bar maps a total range of $\pm 1\%$ in Figures A1-A5. Regions of the detector with deviations $>1\%$ are annotated on the plots. For the UV filters (F218W, F225W, F275W, F280N) obtained in ambient conditions, systematic offsets were found in the aperture photometry between chips, so the variation was instead computed relative to the mean value for each chip. Flux residuals for these filters are presented in Figures A6-A9, where the color bar now maps a total range of $\pm 3\%$ and with values deviating by more than 1% annotated on the plot as before.

The figures represent photometric residuals measured using a 10-pixel aperture, although photometry was performed for a range of apertures from 5-20 pixels. In Figure 4, the rms flux variation (in percent) over all detector positions is plotted as a function of aperture radius for the F336W filter. Inside of 10 pixels, spatial changes in the shape of the PSF across the detector and temporal variations due to telescope breathing are thought to be the cause of the increased rms. The rms reaches a minimum value at 10 pixel radius and increases gradually for larger radii.

Table 2 gives the photometric repeatability of the eight UVIS filters as the standard deviation and the peak-to-peak range of the individual stepped measurements. For a subset of filters (e.g. the flats obtained in vacuum conditions), the table compares photometry derived from calibrated data (FLT) corrected for varying pixel area and from drizzled (DRZ) data products, with the two methods differing by $<0.1\%$. For comparison, the Poisson-limit ($1/\sqrt{N_{\text{electrons}}}$) has been computed for each star as a lower limit to the photometric repeatability. Table 2 also gives the percent difference in the measured flux between UVIS2 and UVIS1. For the four UV filters, this offset increases from 2.4% (F280N) to 4.8% (F218W) as the filter pivot wavelength decreases. The proposed explanation for this offset is discussed in more detail in Section 5.

Figure 4: RMS flux variation (in percent) versus aperture radius for stepped observations in F336W. The rms residuals reach a minimum in a 10-pixel radius aperture.

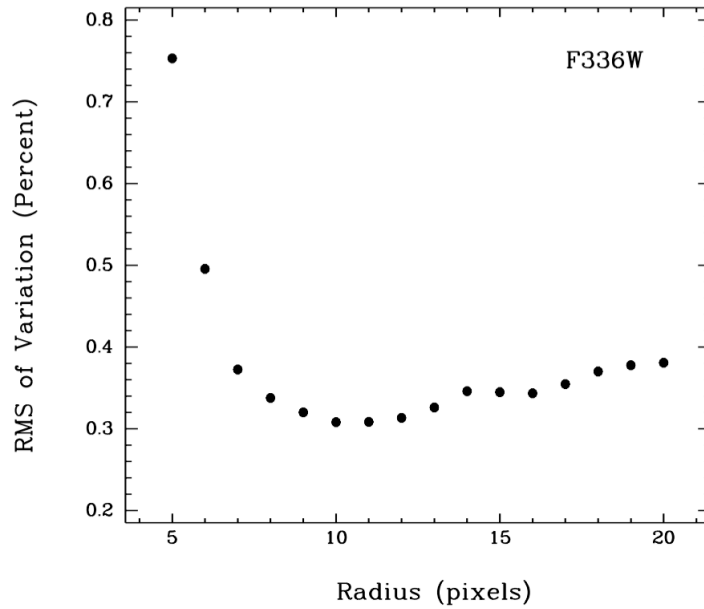
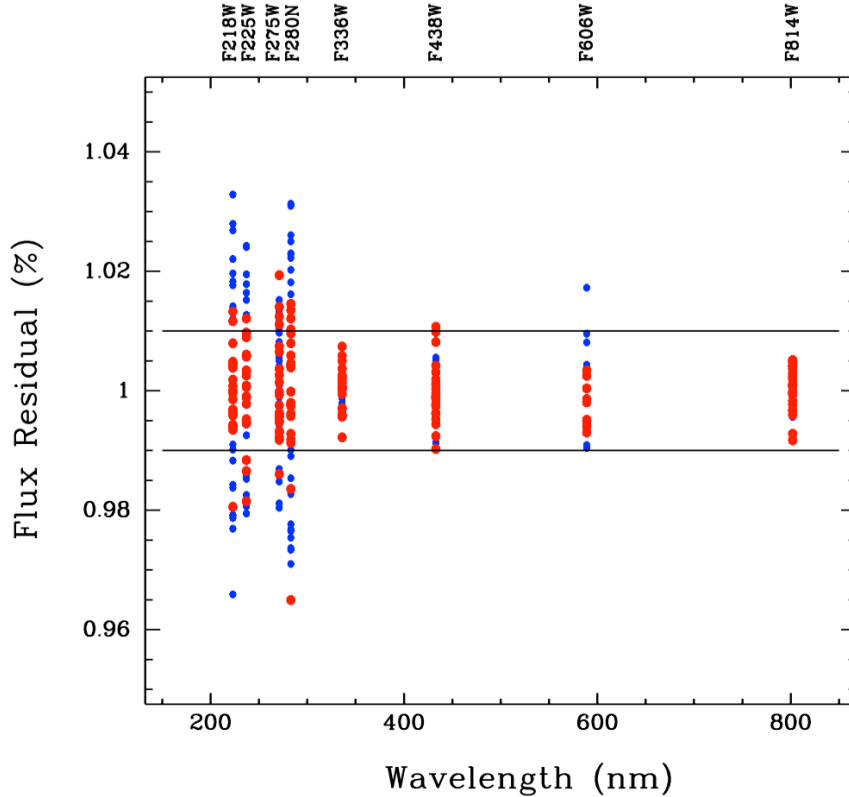


Table 2. The photometric repeatability per filter as the standard deviation and peak-to-peak range, compared to the Poisson error. For a subset of filters, the repeatability was computed from both drizzled (DRZ) and non-drizzled (FLT*PAM) products. In the UV, the UVIS2 photometry is systematically brighter, so the repeatability was computed after removing a constant offset (column 6) in the measured flux between chips.

Filter	Number of Steps	Poisson Error	Stddev (DRZ)	Stddev (FLT)	P2P (DRZ)	P2P (FLT)	Chip Offset
F218W	44	0.2%	1.5 %		6.7 %		4.8 %
F225W	44	0.2%	1.3 %		4.5 %		4.8 %
F275W	50	0.2%	0.9 %		3.9 %		2.5 %
F280N	44	0.2%	1.8 %		6.6 %		2.4 %
F336W	46	0.4%	0.3 %	0.3 %	1.5 %	1.6 %	0.1 %
F438W	50	0.2%	0.5 %	0.4 %	2.0 %	2.0 %	0.0 %
F606W	20	0.3%	0.7 %	0.6 %	2.7 %	2.5 %	0.4 %
F814W	50	0.3%	0.4 %	0.4 %	1.3 %	1.4 %	0.1 %

Figure 5: Flux residual for eight filters computed from drizzled observations in a 10- pixel aperture. Sources stepped across the UVIS1 detector are shown in blue and across the UVIS2 detector in red. For the UV filters, a constant offset between chips has been removed. The remaining residuals are significantly larger for UVIS1, which has a stronger crosshatch pattern in the flats than UVIS2. The horizontal lines indicate $\pm 1\%$ deviation.



The percent variation relative to the mean flux for each standard is plotted as a function of the filter pivot wavelength in Figure 5 for all stepped observations. For the four filter flats obtained in vacuum conditions, the majority of points fall within the horizontal lines at $\pm 1\%$. In the UV, much larger deviations up to $\pm 3.3\%$ are found, even after removing the mean chip offset per filter. The measured residuals correlate with the crosshatch pattern in the flats, e.g. stars falling on low-sensitivity regions in the flat have systematically lower observed flux. The residuals are larger for UVIS1, where the crosshatch pattern is noticeably stronger in the flat. Mack (2016b, *in prep*) use this measured correlation to correct for spatial residuals in the UV flats with detector temperature.

For F336W, F438W, and F814W, the photometric repeatability is better than 0.5% rms and 2.0% peak-to-peak. Variations in the F606W filter are slightly larger at 0.7% rms and 2.7% peak-to-peak. These values in Table 2 and Figure 5 reflect only the second set of observations with longer 2.0 second exposures. The first set of F606W observations used the bright standard G191B2B and short 0.7 second exposures. Variations of $\pm 2\%$ across the detector (Figure A3) were surprising since the flat for this filter was derived using a similar methodology as for the other broad filters and since Omega-Centauri has a large population of red stars for computing the L-flat. The second set of observations used a fainter white dwarf (GD71), longer exposures, and an additional 12 electrons of post-flash to mitigate

CTE losses. Sampling a subset of the original detector positions, Figure A4 shows a slight decrease in the rms and peak-to-peak range compared to Figure A3. This suggests that shutter repeatability is likely part of the cause of the variation in the short exposures. However, we note that spatial residuals have some similarities between the two sets with residuals >1 tending to fall in the upper left corner and <1 in the lower right.

One possible explanation is that the F606W filter is much broader than the other filters, with a rectangular width of nearly 2200 Angstroms, and may be more sensitive to color terms. For example, the spatial response of the detector may be slightly different when measuring blue versus red sources, and that the mixed stellar population in Omega-Centauri may complicate the process of computing low-frequency corrections from dithered data.

V. CTE Effects

The stepped observations were obtained using custom subarrays, so the standard CTE correction software will not work for these data. To estimate the impact of CTE losses on the spatial residuals, we examine two filters with the smallest spatial variation, F336W and F814W which sample both blue and red wavelengths. The mean flux in Figures A1 and A2 appears systematically lower near the UVIS chip gap. For example in F814W, the blue point (259, 2310) at the bottom left corner of UVIS1 has a flux residual of 0.993 with respect to the mean. The drizzled image of the source is shown in Figure 6, where a large CTE-tail can be seen extending downward to the edge of the subarray.

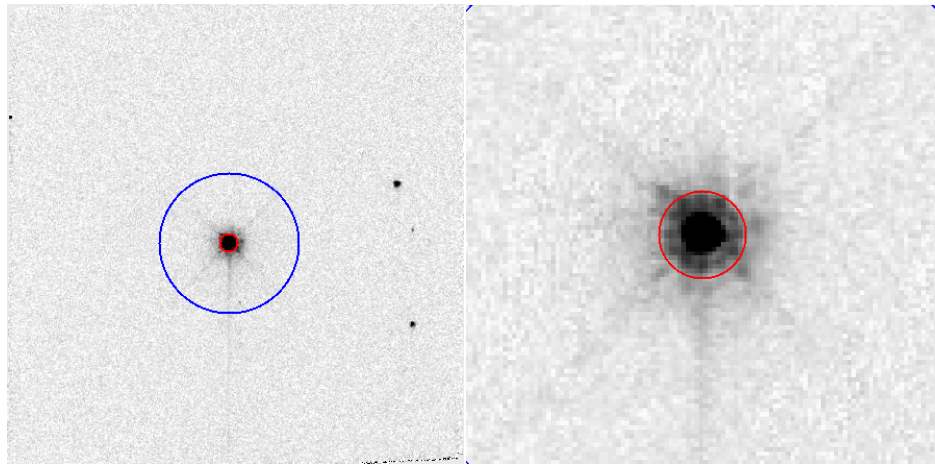


Figure 6: F814W image `ibwh01040_drz.fits` at detector position ($x=259$, $y=2310$) in a 500x500 pixel box (left) and a 100x100 pixel box (right). At the bottom of UVIS1 (near the chip gap), the source has a CTE tail extending nearly to the edge of subarray. The blue circle marks the inner sky annulus at $r=75$ pixels, and the red circle marks the 10 pixel radius used for aperture photometry, which just encloses the first Airy ring.

Figure 7 plots the flux residual versus the number of Y-transfers for F336W and F814W, with a linear fit spanning a total range of 0.5% and 0.8% respectively. This implies that CTE losses are responsible for some of the measured variation in flux across the detector and that the values reported in Table 2 are an upper limit on the error of the flats themselves. For example, after subtracting a linear fit to the CTE from the data points, the F336W residuals drop from 0.31% to 0.28% rms and from 1.52% to 1.21% peak-to-peak

and the F814W residuals drop from 0.35% to 0.28% rms and from 1.34% to 1.11% peak-to-peak. While the F336W filter typically has a lower sky background than the F814W filter and therefore a larger predicted CTE loss, the F814W observations were obtained ~ 1.5 years later. Thus, the steeper slope in the F814W fit is interpreted to be a result of increased radiation damage of the UVIS detector in the 12707 program data compared to 12090.

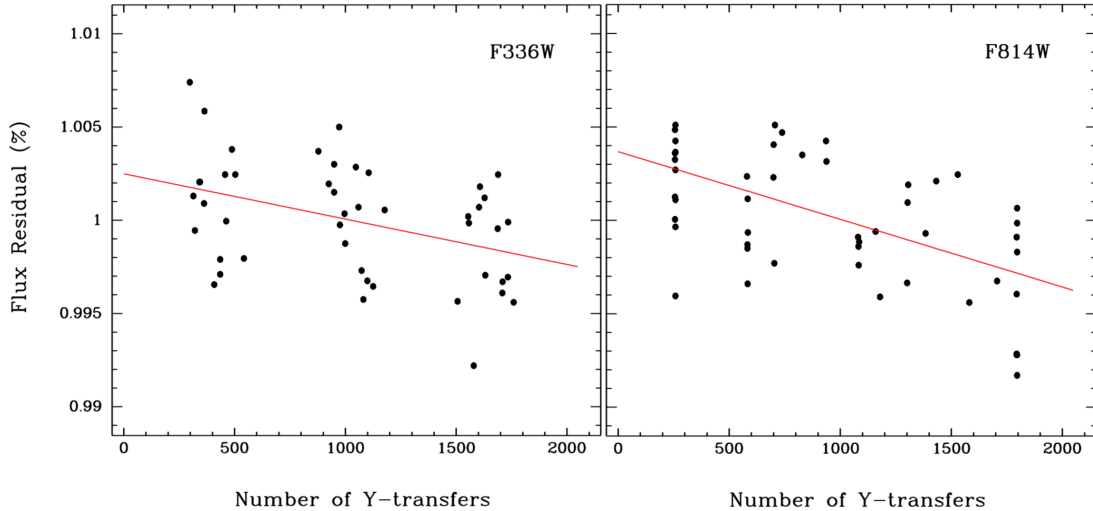


Figure 7: Flux residual (percent) versus number of Y-transfers for F336W (left) and F814W (right) observations. The red lines show linear fits to the data spanning a total range of 0.5% and 0.8%, respectively. This correlation is interpreted as CTE contributing to the spatial variation in the measured flux.

VI. Color Terms

A significant offset in the measured flux between chips is found for the UV filters, e.g. a source falling on UVIS2 has a higher count rate than when it falls on UVIS1. Table 2 shows that this measured offset increases as the filter pivot wavelength decreases. The two UVIS detectors were manufactured in different batches, and UVIS2 achieves higher sensitivity in the UV than UVIS1 by 30%, 21%, 5%, and 2% for F218W, F225W, F275W, and F280N, respectively (Brown 2008). The flats correct for any inherent QE offsets such that dithered photometry of Omega Cen is continuous across the detectors, but this approach assumes that the sensitivity of each detector is independent of spectral type. The measured offsets for the stepped data, however, suggest that the UV filters may indeed depend on the color of the source, since the average population of Omega Cen is significantly redder than the white dwarf standards. We test this hypothesis by separating the cluster stars into four groups based on color and looking for any offsets in the measured photometry as the stars are moved between the two detectors.

For the two UV filters (F225W, F275W) with observations of Omega Cen, we selected exposures oriented 95 degrees from one another (i.e. 3 months apart) from program 11911 to study the effect of moving half of the stars from one detector to the other. These test datasets are summarized in Table 3. As done for the L-flats, aperture photometry was performed in a 5 pixel radius and then corrected to the standard 10 pixel aperture using a 9x10 spatial PSF library adjusted to match the mean focus in each image (Bellini & Bedin, 2009; Anderson et al. 2006).

Using the STMAG zeropoints for 0.4" aperture, the color-magnitude diagram (CMD) was constructed and used to select sources by their observed color and apparent brightness. Figure 8 shows the selected samples of blue, green, yellow, and red stars while Table 4 describes the characteristics of each population. Since the measured chip offset in F275W offset is $\sim 2.5\%$ for the stepped data, only sources with photometric errors < 0.025 mag were selected to minimize scatter in the magnitude differences. Note that the ‘blue’ population is close in color to the HST standards (primarily white dwarfs), and the ‘yellow’ population is representative of the mean color of Omega-Cen.

Table 3. UV exposures of Omega Cen used to test for color terms in UVIS1 versus UVIS2.

Filter	Rootname	Date	Orient	Exptime
F225W	ibc301r3q ibc304wcq	Jan 2010 Apr 2010	150 245	900
F275W	ibc301qtq ibc304v8q	Jan 2010 Apr 2010	150 245	800

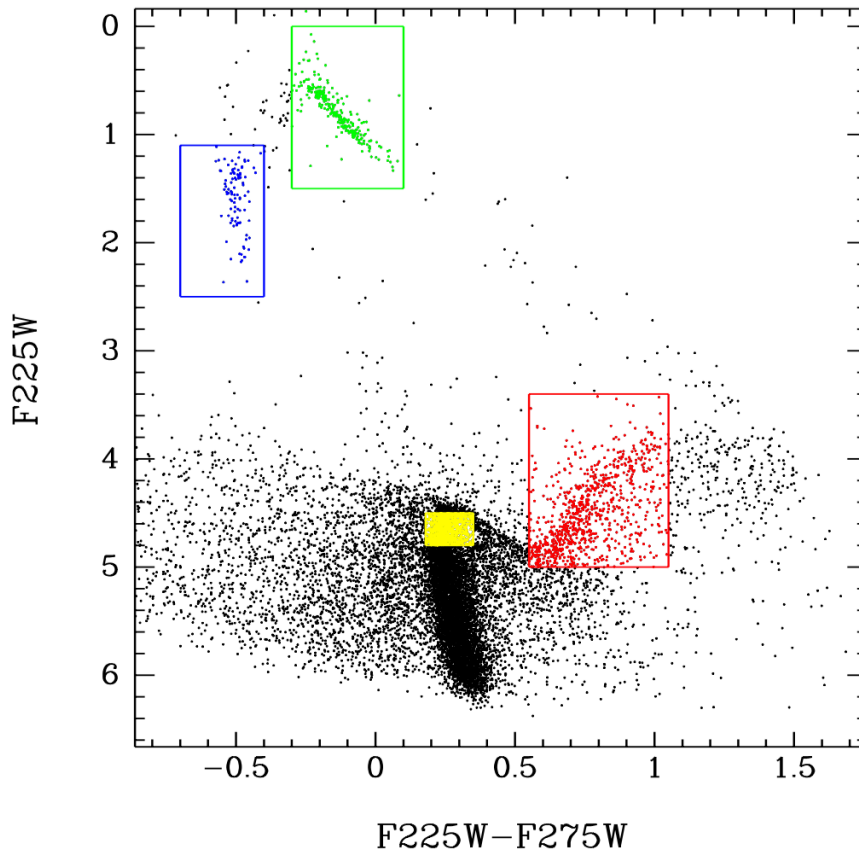


Figure 8: UV color-magnitude diagram for Omega Centauri. Sources were selected by color to quantify photometric offsets between UVIS1 and UVIS2.

Figure 9 plots the F225W magnitude difference versus y-position for the two rotated exposures listed in Table 3, where blue, green, yellow, and red populations are shown from top to bottom. With a 90 degree rotation, ~half of the stars cross from one chip to the other, and only this set of stars are shown in the figure for clarity. Note that only the yellow stars are continuous across the two chips and that the blue and red populations show a systematic offset at $y \sim 2048$ pixels, albeit in opposite directions.

The ‘optimal’ photometric offset for each population is determined as the value that minimizes the scatter in delta-magnitude across the two detectors. A large range of constant offsets was tested, with a step size of 0.001 magnitudes. While the optimal offset was determined using the full set of stars, only those stars that cross from one chip to the other are shown (right panel). This offset is given in the last two columns of Table 4 for F225W and F275W as a function of source color. This is also plotted in Figure 10, with a linear fit to points in each filter overplotted on the graph. Horizontal error bars show the color range sampled in by each population. Vertical error bars (dMAG) may be estimated as the mean photometric error of the population, divided by the square root of the number of individual measurements. These errors are smaller than the points on the figure, so are not plotted.

Because the red leak for these two UV filters is non-negligible, the red points were not included in the fit. The Instrument Handbook (Dressel, 2015) estimates the red leak as 1.8% in F225W and 0.3% in F275W for a 4,000 K blackbody. This is roughly consistent with the measured offsets in the red points (0.7% in F225W and 0.3% in F275W) from the best fit lines to the blue, green and yellow points in Figure 10.

Table 4. Omega Cen populations used to test for color terms in the UV filters.

Color	Number of stars	Color (F225W-F275W)	Mag (F225W)	Mean Error (mag)	F225W ‘Delta’ (mag)	F275W ‘Delta’ (mag)
Blue	100	-0.60 .. -0.40	1.1 .. 2.5	0.002	-0.041	-0.019
Green	265	-0.30 .. 0.10	0.1 .. 1.5	0.002	-0.023	-0.012
Yellow	1000	0.18 .. 0.35	4.5 .. 4.8	0.013	-0.005	-0.006
Red	870	0.55 .. 1.05	3.4 .. 5.0	0.010	+0.027	+0.006

The measured offset between the blue and yellow populations in Omega Cen is 0.036 mag (3.4%) for F225W, and 0.013 mag (1.2%) for F275W. This supports the hypothesis that the offset in the stepped photometry for F225W and F275W (4.8% and 2.5%, respectively, from Table 2) is due to color differences between the hot, blue HST standards and the average population of stars in Omega Cen used to compute the L-flats. For users performing photometry of blue sources or mixed age populations with the UV filters, the current UVIS calibration (flat fields and zeropoints) will have errors at this level.

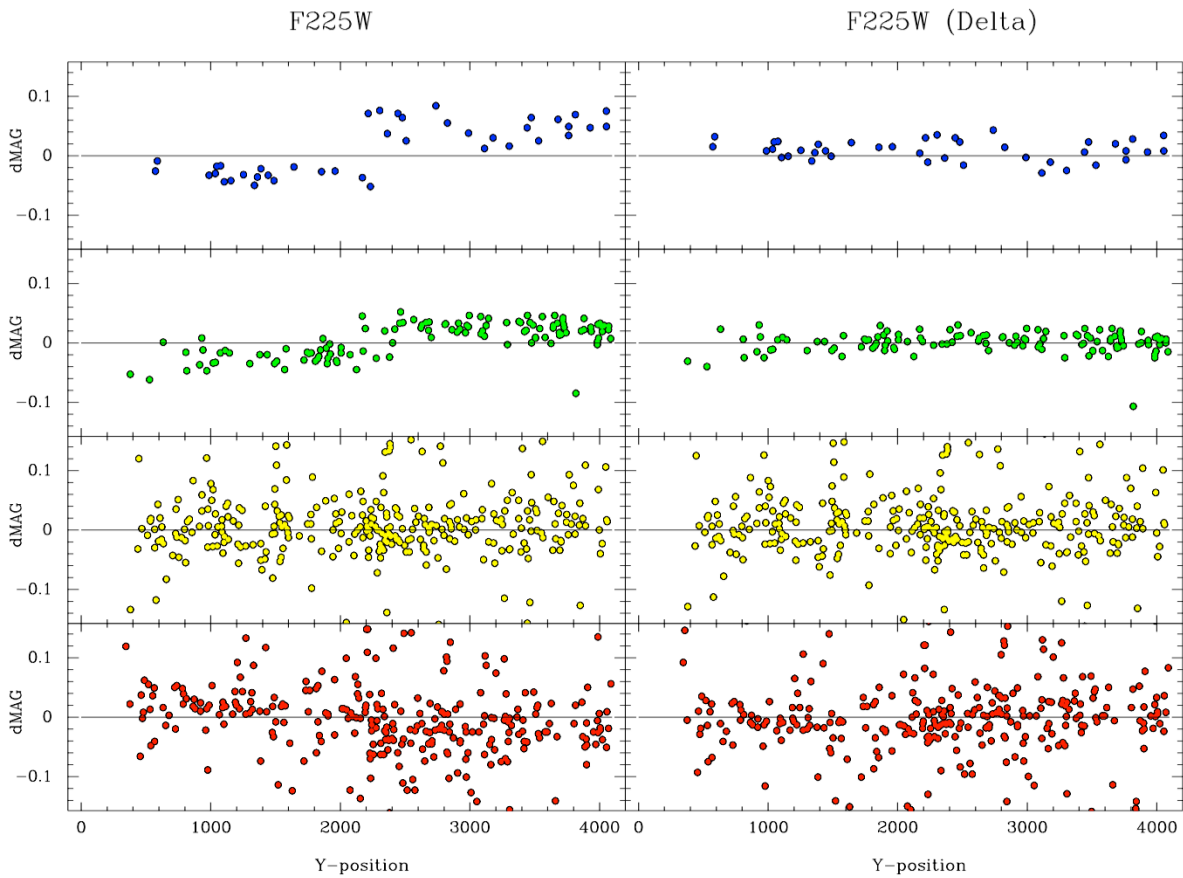


Figure 9: F225W delta-mag versus Y-position for stars that cross between UVIS1 and UVIS2. Blue, green, yellow, and red populations (top to bottom) with photometric errors <0.025 mag were selected to look for color terms as stars move between the two UVIS detectors. The left panels show systematic offsets at $Y \sim 2048$ for all but the yellow population. A constant magnitude offset, which minimizes the scatter in delta-magnitude for each population, has been applied in the right panels.

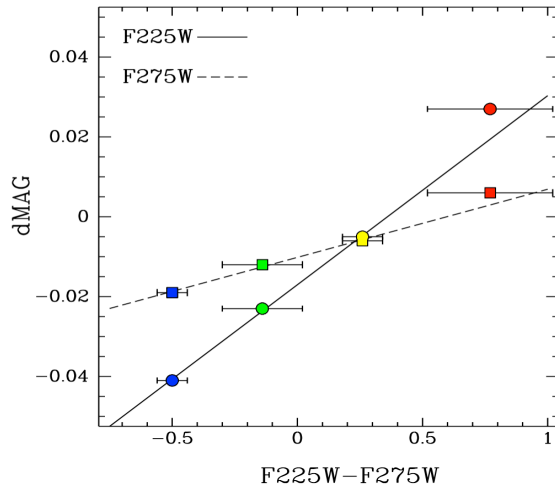


Figure 10: Magnitude offset between chips versus source color, with horizontal bars indicating the color range sampled in the CMD. The solid line is a fit to the F225W filter (circles) and the dashed line is a fit to the F275W filter (squares). The red points are likely impacted by red leak so were not included in either fit.

Conclusions

The spatial repeatability of stepped HST standards has been used to estimate the accuracy of the current set of UVIS flat fields (`v*pfl.fits`) delivered in December 2011. For F336W, F438W, F606W, and F814W, the spatial residuals are $<0.7\%$ rms and 2.7% peak-to-peak. The photometric residuals are an upper limit on the error in the flats which suffer from CTE losses at a level of $0.5\text{-}1.0\%$.

The UV flats were obtained in ambient conditions during ground testing and show larger spatial residuals up to 1.8% rms and 6.7% peak-to-peak. These residuals correlate with a crosshatch pattern in the flats on scales of 10^3 's of pixels. A forthcoming ISR will describe using these data to construct a model to correct the UV flats.

For the UV filters, photometry in the UVIS2 chip is systematically brighter than UVIS1, and this difference increases as the filter pivot wavelength decreases. The flats attempt to correct for QE offsets between the two chips using dithered stellar photometry of Omega Cen, but the average cluster population is significantly redder than the stepped HST standards (primarily white dwarfs). Separating the cluster population by color, we measure offsets in the photometry as stars are dithered from one chip to the other. We measure a linear trend in the chip offset with color, consistent with the offsets measured in the stepped photometry. This suggests that the UV filters have significant color terms up to 5% .

A new chip-dependent solution for the two UVIS detectors is in preparation (Deustua et al., 2016). This new solution will remove any inherent sensitivity offsets between chips from the flats themselves and instead scale the two chips by flux ratio of hot white dwarf standards measured for UVIS1 and UVIS2 separately. An additional red HST standard (P330E) will be used to compute color terms for all UVIS filters and will provide a cross-check to color terms measured from the dithered Omega Cen observations.

Acknowledgements

The authors are grateful for Peter McCullough and Ralph Bohlin for reviewing this ISR and providing helpful feedback. We also thank Susana Deustua for useful discussions on photometry of HST white dwarf standards which were used to compute both the UVIS zeropoints and the spatial accuracy of the flats.

References

- Anderson, J., Bedin, L. R., Piotto, G., Yadav, R. S., & Bellini, A. 2006, *A&A*, 454, 1029
- Anderson, J., Mackenty, J., Baggett, S., and Noeske, K., 2012, “The Efficacy of Post-Flashing for Mitigating CTE-Losses in WFC3/UVIS Images,” unpublished white paper, http://www.stsci.edu/hst/wfc3/ins_performance/CTE/ANDERSON_UVIS_POSTFLASH_EFFICACY.pdf
- Bellini, A. & Bedin, L. R. 2009, *PASP*, 121, 1419
- Baggett, S. 2007, WFC3 ISR 2007-14, “WFC3 Ambient-2 Testing: Calibration Subsystem Performance”
- Brown, T. M. 2008, WFC3 ISR 2008-48, “WFC3 TV3 Testing: System Throughput on the UVIS Build 1’ Detector”
- Deustua, S. et al. WFC3 ISR *in prep*, “UVIS 2.0: Photometric Calibration”
- Dressel, L., 2015. “Wide Field Camera 3 Instrument Handbook, Version 7.0”
- Hilbert, B. 2010, WFC3 ISR 2009-25, “WFC3 SMOV Program 11427: UVIS Channel Shutter Shading”
- Kalirai, J., et al. 2009, WFC3 ISR 2009-31, “WFC3 SMOV Proposal 11450: The Photometric Performance and Calibration of WFC3/UVIS”
- Mack, J., Sabbi, E., & Dahlen, T. 2013, WFC3 ISR 2013-10, “In-flight Corrections to the WFC3 UVIS Flat Fields”
- Mack, J. 2016a, WFC3 ISR *in prep*, “Combining Small Datasets with AstroDrizzle”
- Mack, J. 2016b, WFC3 ISR *in prep*, “UVIS 2.0: Ultraviolet Flats”
- McCullough, P. 2011, WFC3 ISR 2011-16 , “Geometric model of UVIS window ghosts in WFC3”
- Sabbi, E. 2008, WFC3 ISR 2008-12, “UVIS CASTLE Photometric Filter Flat Field Atlas”
- Sabbi, E., Dulude, M., Martel, A.R., Baggett, S., & Bushouse, H. 2009, WFC3 ISR 2008-46, “WFC3 Ground P-flats”
- Sabbi, E. & Bellini, A. 2013, WFC3 ISR 2013-11, “UVIS PSF Spatial and Temporal Variations”
- Wong, M. 2010, in “The 2010 STScI Calibration Workshop”, ed. S. Deustua and C. Oliveira (Baltimore: STScI), 183, “Fringing in the WFC3/UVIS Detector”

Appendix A: Spatial Residuals

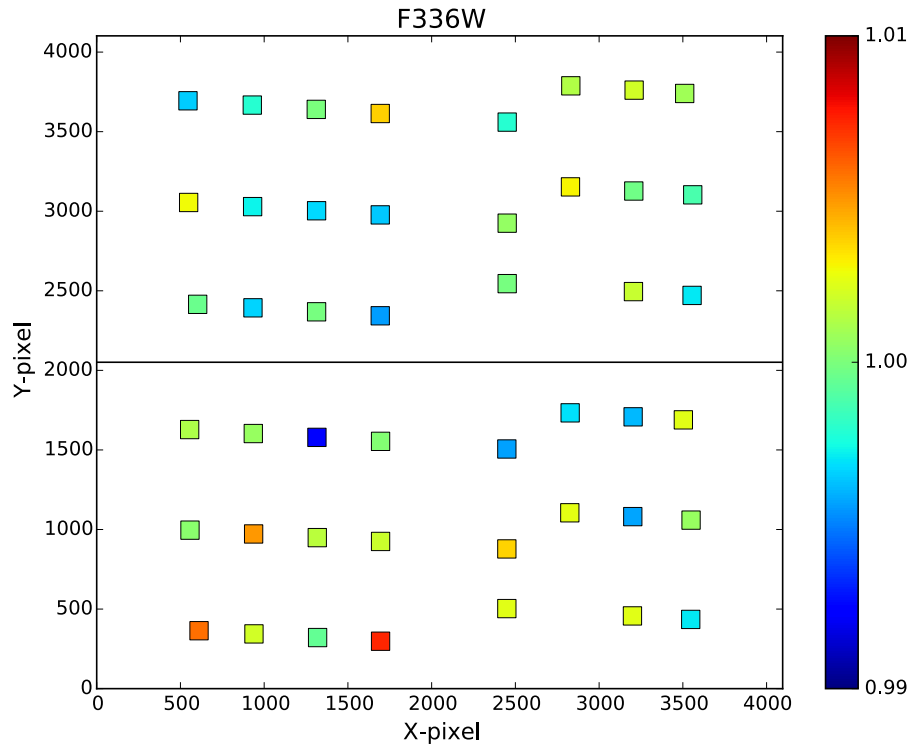


Figure A1: F336W percent variation relative to the mean flux for GD153.

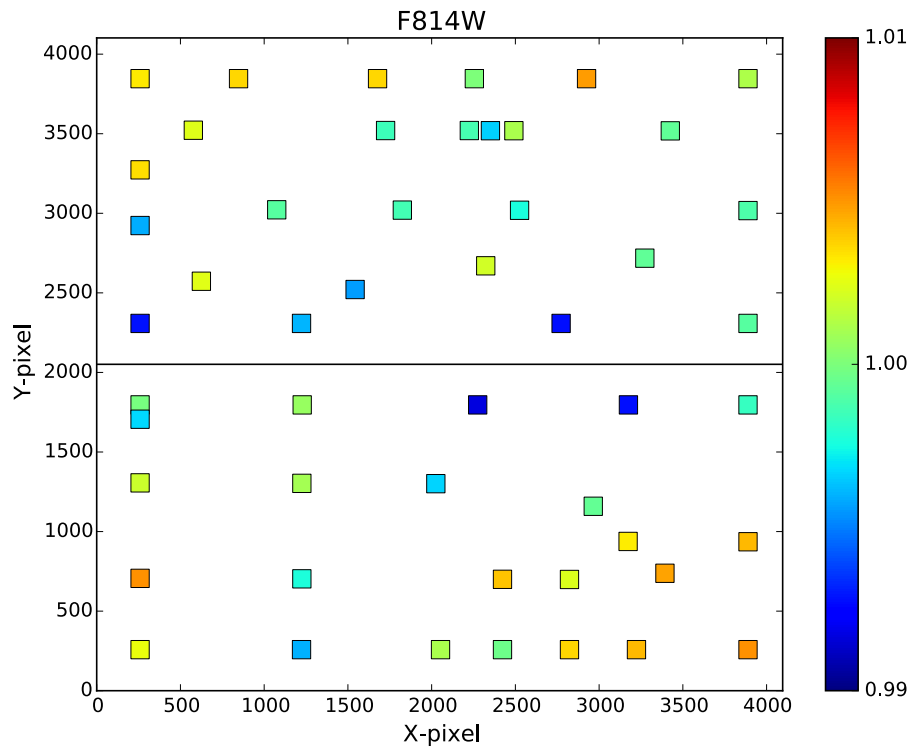


Figure A2: F814W percent variation relative to the mean flux for G191B2B.

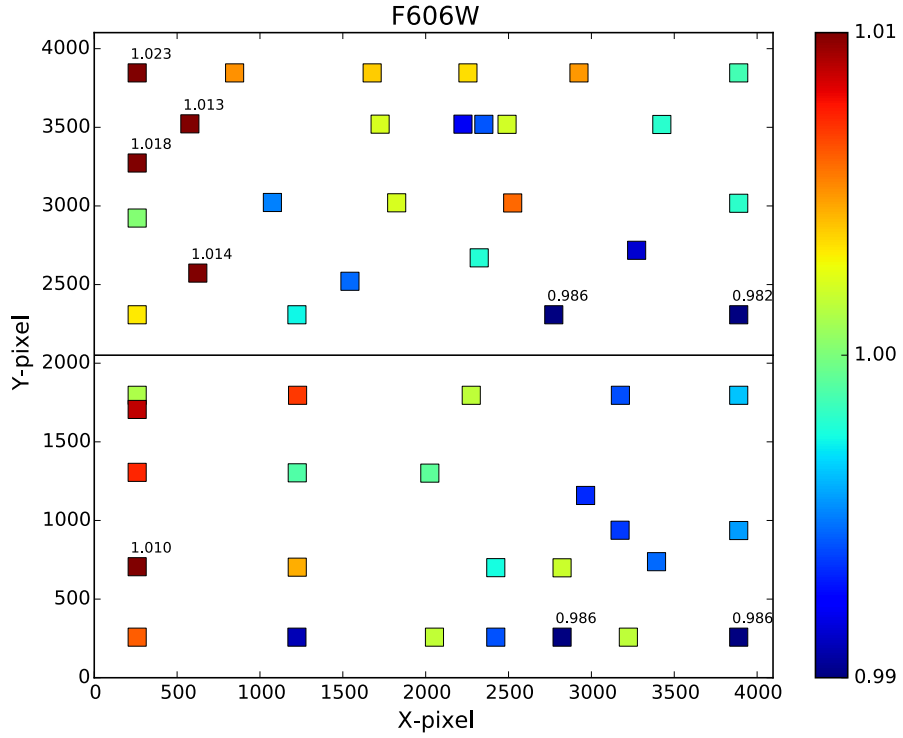


Figure A3: F606W percent variation relative to the mean flux for the short 0.7 second exposures of G191B2B. The short exposures likely contribute to the increased variation.

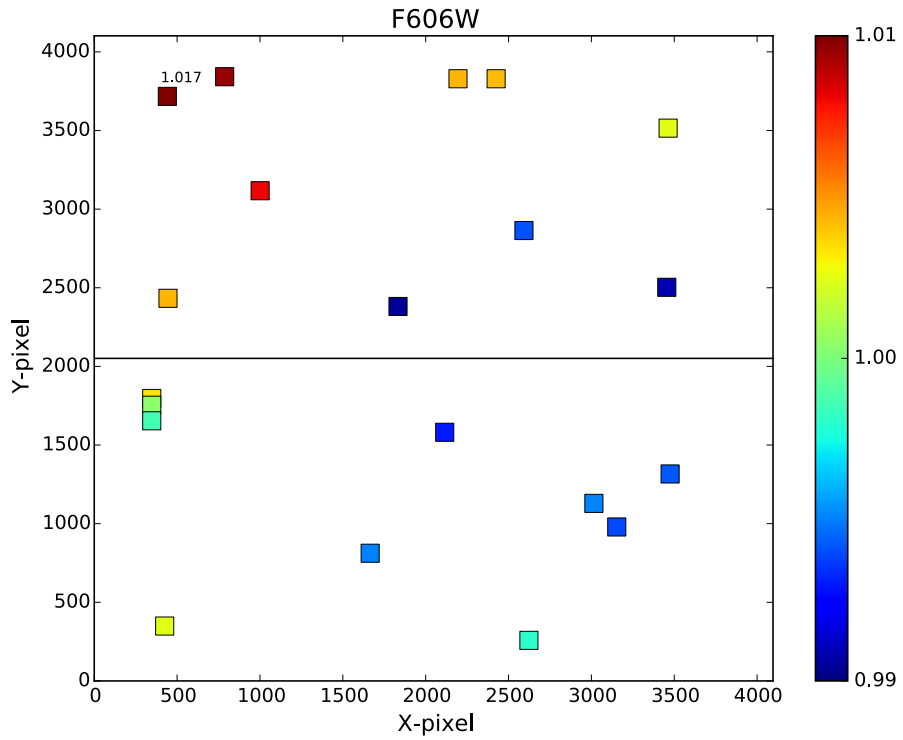


Figure A4: F606W percent variation relative to the mean flux for the longer 2.0 second exposures of GD71.

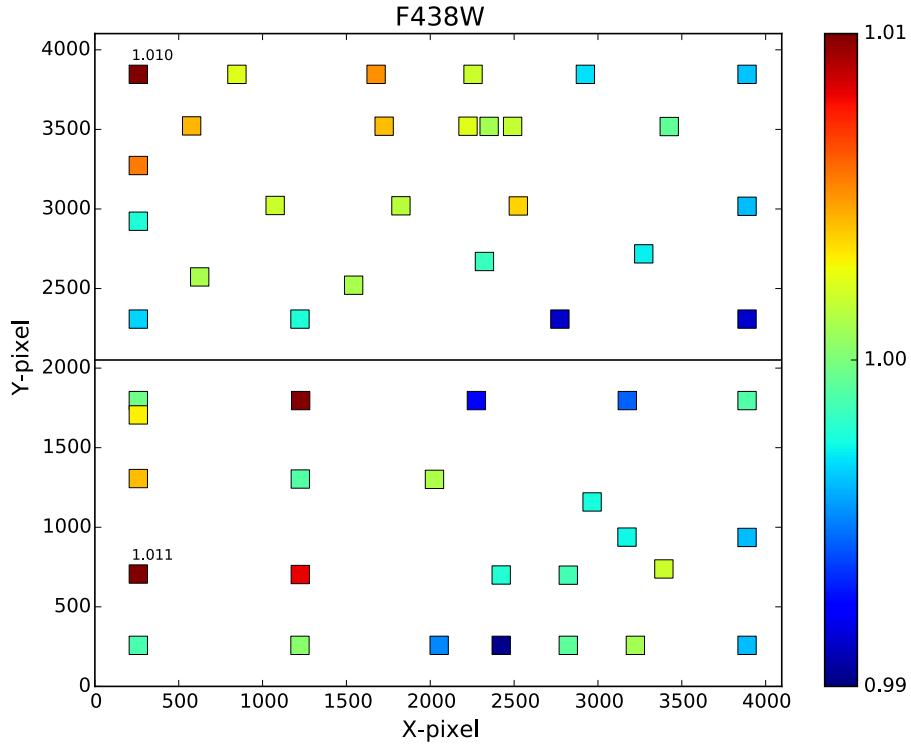


Figure A5: F438W percent variation relative to the mean flux for G191B2B.

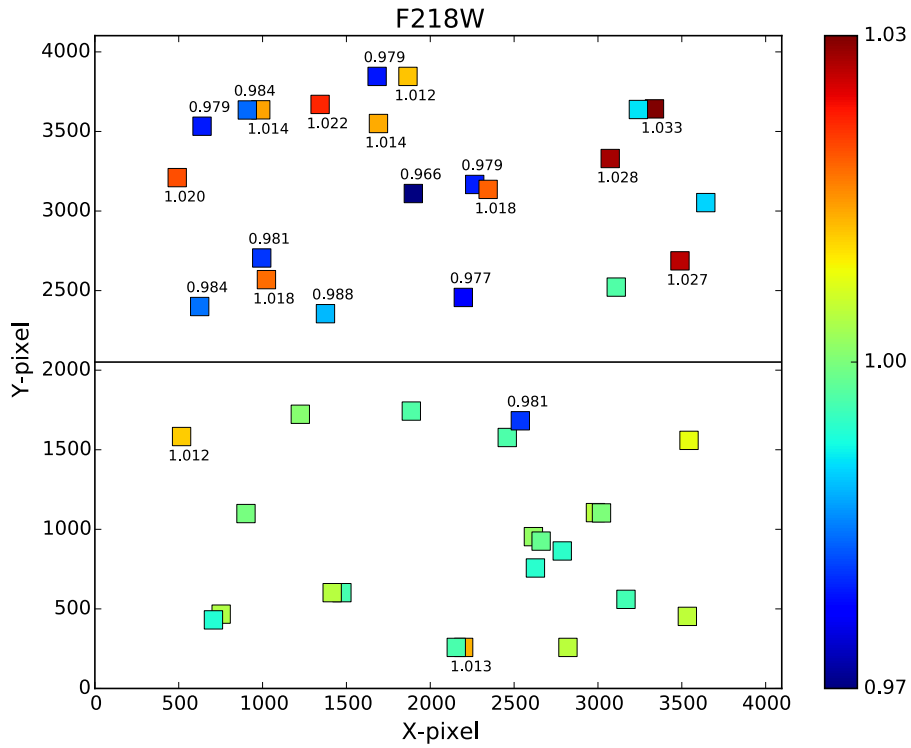


Figure A6: F218W percent variation relative to the mean flux per chip for G191B2B.

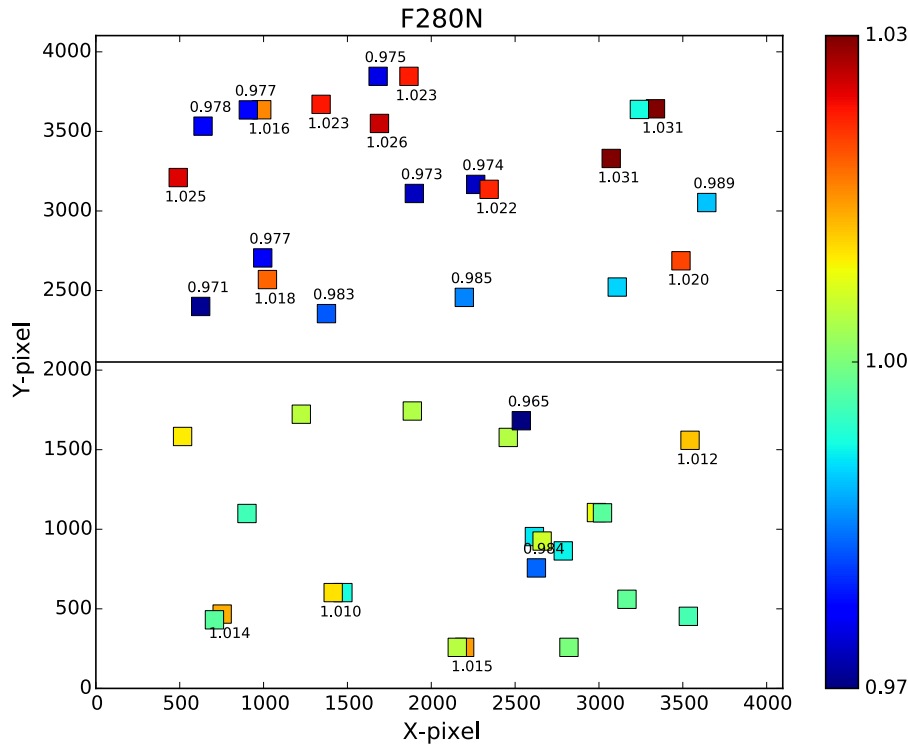


Figure A9: F280N percent variation relative to the mean flux per chip for BD+75D325.

Appendix B: Subarray Distortion Correction

The python code ‘subarray_regions.py’ is useful for converting subarray observations to full-frame coordinates. Originally written by Howard Bushouse (STScI, Science Software Branch), it has been adapted to print out the syntax for running ‘imcalc’ in PyRAF to multiply the subarray *flt.fits frame by the appropriate region of the pixel area map. This allows the user to perform photometry directly on undrizzled images by correcting for the effects of distortion. The code requires both the *flt.fits and the *spt.fits data products as input.

The output file ‘pamlist.txt’ prints out call to imcalc for each image in the input directory. For example:

```
iraf.imcalc(input='ic5p03fcq_flt.fits[1],UVIS2wfc3_map.fits[1][2178:2689,1321:1832]',
output='ic5p03fcq_pam.fits', equals='im1*im2')
```

The output file ‘cornerlist.txt’ gives the subarray corners (and chip) for each image, which is useful for calculating the source position in full-frame coordinates. For example:

```
>> ic5p03fcq_flt.fits 2178 1321 2
```

To get the full-frame coordinates, the user may simply add the measured star position in the subarray, for example (257, 241) to the position of the corner. This maps to (2435, 1562) in the calibrated *flt.fits image on UVIS2. The python code is appended below.

```
"""
subarray_regions.py
"""

import pyfits, glob
import numpy as np

flist = glob.glob("*flt.fits")
cornerlist = []
pamlist = []

for file in flist:
    root = file[0:file.find('_flt')]
    flt = root + '_flt.fits'
    spt = root + '_spt.fits'

    uvis_a2_size = 2051
    serial_over = 25
    chip_xsize = 2051
    ir_overscan = 5

    fd1=pyfits.open(flt)
    fd2=pyfits.open(spt)

    detector=fd1[0].header['DETECTOR']
    subarray=fd1[0].header['SUBARRAY']
    xcorner=int(fd2[1].header['XCORNER'])
    ycorner=int(fd2[1].header['YCORNER'])
    numrows=int(fd2[1].header['NUMROWS'])
    numcols=int(fd2[1].header['NUMCOLS'])
    ccddchip=int(fd1[1].header['CCDCHIP'])

    sizaxis1 = numcols
    sizaxis2 = numrows

    if (xcorner==0 and ycorner==0):
        cornera1 = 0
        cornera2 = 0
        cornera1a = cornera1 + 1
        cornera1b = cornera1a + sizaxis1 - 1
        cornera2a = cornera2 + 1
        cornera2b = cornera2a + sizaxis2 - 1
    else:
        if detector == 'UVIS':
            cornera1 = ycorner
            cornera2 = uvis_a2_size - xcorner - sizaxis2
            if xcorner >= uvis_a2_size:
                cornera2 = cornera2 + uvis_a2_size
```

```

corner1a = corner1 + 1 - serial_over
corner1b = corner1a + sizaxis1 - 1
corner2a = corner2 + 1
corner2b = corner2a + sizaxis2 - 1

if corner1a < 1:
    corner1a = 1
if corner1b > 4096:
    corner1b = 4096

else:
    corner1 = ycorner - ir_overscan
    corner2 = xcorner - ir_overscan

    corner1a = corner1 + 1
    corner1b = corner1a + sizaxis1 - 11
    corner2a = corner2 + 1
    corner2b = corner2a + sizaxis2 - 11

cornerlist.append([flt,corner1a,corner2a,ccdchip])

pamlist.append(["iraf.imcalc(input="",flt,"[1],UVIS", ccdchip,
    "wfc3_map.fits[1][",corner1a,":",corner1b,",",corner2a,":",
    corner2b,")',output="",root,"_pam.fits',equals='im1*im2')"])

fd1.close()
fd2.close()

np.savetxt("cornerlist.txt",cornerlist,fmt='%s',delimiter=' ')
np.savetxt("pamlist.txt",pamlist,fmt='%s',delimiter=")

```